



# Survey of the near wake of an axial-flow hydrokinetic turbine in quiescent conditions

Ethan E. Lust<sup>\*</sup>, Karen A. Flack, Luksa Luznik

Mechanical Engineering Department, United States Naval Academy, Annapolis, MD, USA



## ARTICLE INFO

### Article history:

Received 26 October 2017

Received in revised form

24 April 2018

Accepted 21 May 2018

Available online 23 May 2018

### Keywords:

Marine current turbine

Flow field

Wake survey

Towing tank

Particle image velocimetry

Aperiodicity

## ABSTRACT

Flow field results are presented for the near-wake of an axial flow hydrokinetic turbine in quiescent flow conditions. The turbine is a 1/25 scale, 0.8 m diameter, two bladed turbine modeled after the Sandia National Laboratory Reference Model 1 Tidal Current Turbine. All measurements were obtained in the large towing tank facility at the United States Naval Academy with the turbine towed at a constant carriage speed and a tip speed ratio corresponding to maximum power production. The turbine is scale independent with respect to lift and very slightly dependent with respect to drag for these conditions ( $Re_{c@0.7R} \approx 4 \times 10^5$ ). The wake velocity field data was obtained using a two-dimensional particle image velocimetry (PIV) system. PIV ensembles were obtained for phase locked conditions. This paper focuses on characterizing the velocity and the mean flow structure in the near wake. Specifically, the downstream evolution of coherent tip vortices shed by the rotor blades were examined. Vortex aperiodicity was shown to increase with downstream distance. The streamwise spacing between adjacent vortex cores was shown to be constant within a diameter downstream of the rotor. Further downstream, significant vortex filament interaction was observed, including leapfrogging. This interaction is thought to be the primary mechanism for wake breakdown and re-energization.

Published by Elsevier Ltd.

## 1. Introduction

According to Hermann [1], approximately 3.7 TW of tidal exergy is dissipated worldwide, 2.5 TW of which is dissipated in the shallow ocean and continental shelves. Current dissipation as a consequence of collection for energy services amounts to approximately 500 MW (0.014%), primarily from barrage systems. In addition to being abundant, tidal exergy is clean and sustainable.

A number of technologies have been developed to collect tidal exergy of which axial-flow (also called horizontal-axis) hydrokinetic turbine technology is the most mature based on total installed capacity [2]. Still, the amount of exergy collected is quite small compared to the considerable size of the resource. The primary reason for this is the current high relative cost of electricity as compared with other, more traditional, technologically-mature sources.

In an effort to spur development of marine hydrokinetic turbine technology and reduce the associated cost of electricity, the U.S.

Department of Energy developed and promulgated six open-source marine hydrokinetic energy converter devices, including Reference Model 1 (RM1) a tidal current turbine, shown in Fig. 1. It called for industry, academic, and national lab partners to create open-source products including the development and dissemination of physical model data sets for validating design modeling tools [3]. These tools could then be used to predict turbine performance, reducing the uncertainty associated with design and development, thereby reducing the cost of implementation, and thus making the technology more cost-competitive.

Large scale implementation of hydrokinetic devices will require sites with an array of turbines. One of the major questions is where to position multiple turbines in an array arrangement to maximize power production. To answer this question, the turbine wake must be characterized as the spacing and orientation of adjacent turbines is primarily dependent on the state of the flow immediately upstream of each respective turbine.

A number of experimental studies have focused on wake velocity measurements in the vicinity of a single axial flow turbine. Results show that the influence of the turbine appears to extend as far as two rotor diameters (2D) upstream of the rotor plane [4]. Flow swirling in this region has also been observed, prior to passing

<sup>\*</sup> Corresponding author.

E-mail address: [lust@usna.edu](mailto:lust@usna.edu) (E.E. Lust).

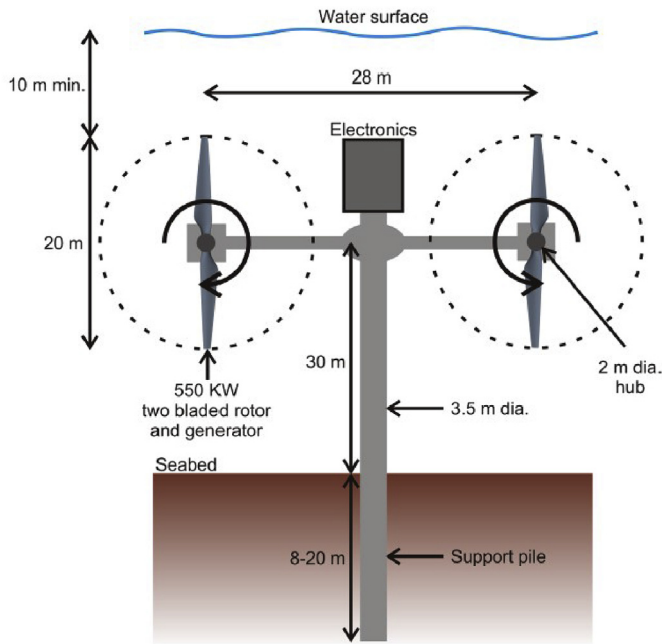


**Fig. 1.** Reference Model 1 (RM1) promulgated by the U.S. National Renewable Energy Laboratory.

through the rotor plane [5]. Downstream of the turbine, observations confirm Froude's theory which predicts the velocity in the near wake ( $x/D < 2$ ) to be approximately one-third that of the free stream, recovering in the far wake ( $x/D > 2$ ) [e.g. Ref. [6]].

Wake expansion caused by the downstream velocity deficit is well documented in the wind turbine literature and is also observed in marine turbine experiments [4,7–9]. Expansion of the shear layer is shown to be proportional to the  $1/3$  power of the streamwise distance [4]. Allo et al. [9] showed the maximum radial expansion to be approximately  $1.3R$  at maximum performance, about 10% lower than the  $\sqrt{2}R$  predicted by Betz. Mycek et al. [10] state that the wake is not axis-symmetric, an observation also made by Tedds, Owen and Poole [11], however, it's not clear if the asymmetry is a result of blockage caused by either the free surface above or the channel floor below, or the influence of the support structure. Chamorro et al. observed approximate azimuthal uniformity in the near wake of the turbine and wake rotation in the direction opposite the turbine [4].

Several studies included particle image velocimetry (PIV) measurements taken at a constant turbine blade angular position or phase showing coherent blade tip vortices within 2D downstream of the turbine. Within 1D, vortices were observed to be strong and spatially stable [4], becoming less concentrated as they convect downstream [5], and decreasing in concentration and positional stability at downstream distances of 1.5D to 2D [4,6,12]. The distance between the adjacent helical vortex filaments in this region was observed to be fairly constant by Okulov [6] although the opposite was observed by Chamorro et al. [7]. The difference in the two observations may depend on whether or not meandering, also called aperiodicity, was accounted for. Allo et al. [9] argue that tip vortex instability is activated by the deformation and incorporation of the blade wake into the tip vortex, causing it to grow. Using the average spatial diameter of the Q-isosurfaces, Chamorro et al. [7] observed that vortex core diameters were of the same order of magnitude as the blade chord.

Several studies have also investigated the instability modes of the helical tip vortex in an effort to predict the streamwise point at

which the near-wake structure begins to break down and subsequently re-energize. Widnall [13] found three instability modes: a short-wave mode, a long-wave mode, and one mutual inductance mode relating to the streamwise distance between adjacent filaments. Predictions were confirmed for marine propellers by Felli et al. [14] who showed that the mutual inductance mode has the greatest impact on wake stability. Their observations were confirmed for wind turbines by Sherry et al. [15] who also observed that first evidence of mutual inductance occurs at the same non-dimensional downstream distance  $0.6h$  where  $h$  is the helical pitch, a function of the turbine tip speed ratio. Sherry et al. also stated that the breakdown of helical structure in the near wake was influenced by interaction between the root and tip vortices, though this was shown not to occur within 1D by Chamorro et al. [7].

In a pair of related studies, Lignarolo et al. [12,16] posed and addressed a number of important questions regarding kinetic energy transport in the wake region. Of particular interest to the present discussion is the question of what role the tip vortices play in enhancing or inhibiting kinetic energy transport from the mean flow to the wake. They concluded that there is effectively no mixing in the near-wake, the helical tip vortex structure shielding it from re-energization within the first two turbine blade diameters downstream.

Wake characteristics have also been shown to be affected by inflow turbulence such as the wake signature of upstream turbines. Inflow turbulence was shown to increase blade loading fluctuations, shorten the downstream wake recovery distance [8], and heavily influence the shape, length, and strength of the wake [10,17]. The instantaneous power generated by the turbine was shown to be strongly affected by turbulent inflow features below a specified critical frequency. It was also shown that this frequency varied linearly with the angular frequency of the turbine at length scales corresponding to the largest structures in the wake [7].

The goal of the present paper is to collect high spatial resolution velocity data in the near wake of a large-scale model axial-flow hydrokinetic turbine under steady conditions. In addition to providing experimental data for computational model validation, this data can be used to corroborate, and in some cases clarify, the observations discussed in the preceding background. This knowledge can then be applied during the planning process reducing the uncertainty associated with implementation and potentially helping to reduce the cost of electricity for marine renewable energy.

## 2. Materials and methods

The experiments were conducted in the large towing tank at the U.S. Naval Academy which measures 116 m long, 7.9 m wide, and 4.9 m deep. All experimental and data acquisition equipment was mounted to a carriage which was towed for all experiments at 1.68 m/s.

The turbine used in this experiment, shown in Fig. 2, is a two-bladed axial-flow design based on Sandia Laboratories Reference Model 1 Tidal Current Turbine, proposed to measure 20 m in diameter and produce 550 kW in flow speeds of up to 3 m/s (1). The 1:25 scale model turbine measures 0.8 m in diameter. The blades are twisted from  $13^\circ$  at the root to  $2^\circ$  at the tip and tapered from a maximum chord length of 7 cm to a minimum of 2.5 cm. The blades were mounted just aft of a nacelle measuring 8 cm in diameter and were manufactured at the U.S. Naval Academy using a 5-axis computer numerical control milling machine from 6061 Aluminum, selected for its excellent machinability and corrosion resistance. The blades were given a matte black anodized finish to provide contrast for imaging experiments. The blockage ratio, defined as the ratio of the turbine swept area to the towing tank traverse area, was 1.3%, and shown to have a negligible impact on

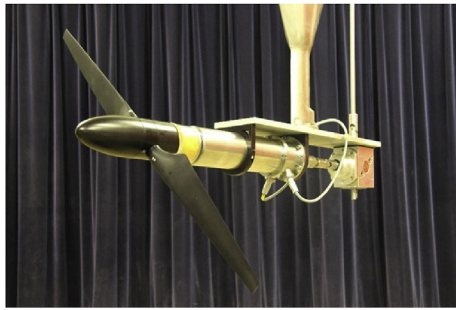


**Fig. 2.** The two-bladed cross-flow hydrokinetic turbine used in the present experiment, shown mounted to the dynamometer with the data acquisition cables for thrust and torque protruding from below.

the performance data for this experiment using the methodology described in Ref. [18]. Further discussion of the performance of this model turbine in quiescent conditions and in the presence of waves can be found in Lust et al. [19]. The impact of biofouling on the performance of this turbine and comparison to blade element method (BEM) model predictions can be found in Walker et al. [20].

The turbine is a geometrically similar 1/25th scale model of RM1, with the exception of the airfoil shape. RM1 features a NACA 63–424 foil, whereas a NACA 63–618 was selected for this experiment for reasons discussed below.

Dynamic similarity for the model turbine is ideally achieved by matching the Reynolds number of the full size turbine because it most readily describes the flow around the turbine blades. For reference, the Reynolds number of RM 1, operating in a current of 0.5–3.0 m/s at a tip speed ratio of 7 is  $2.5 \times 10^6 - 1.5 \times 10^7$ . However, since few facilities with well-controlled flow conditions outside of field test facilities are capable of conducting experiments at this scale, reaching a Reynolds number sufficiently high to achieve independence is generally accepted as a satisfactory criterion for model similarity. In this case, independence is defined as the Reynolds number above which there is no observable change in integral performance characteristics. It should be noted that there appears to be little agreement in the literature as to what parameters to use in the calculation of the Reynolds number for a turbine. With regard to characteristic length, tip chord length [6,8,15,16,21,22], radius [12], and diameter [10,11] are all used. Additionally, both hub velocity [7,8,11,15,21], and relative velocity ( $U_{rel} = \sqrt{U_{hub}^2 + (R\Omega)^2}$ ) at the blade tip [6,15,22] are all used to calculate Reynolds number. This makes direct comparison between studies difficult. It is also difficult to determine the extent to which Reynolds scaling effects may affect observations, but most agree that scaling effects are most pronounced in the near-wake where wake dynamics are a strong function of blade hydrodynamics.

Chamorro, Arndt, and Sotiropoulos [23] conducted an experimental study on a model wind turbine in order to determine what Reynolds number threshold was required for independence with respect to their turbine. In their study they increased the Reynolds number, calculated using the mean flow speed measured at hub height and the turbine diameter as the characteristic length, until the streamwise velocity profiles and second order statistics (i.e. turbulence intensity and Reynolds stress) collapsed onto a single profile for each respective parameter. This approach, however, is unique to each turbine. Gaurier et al. [24] also examined the effects of Reynolds number dependence on the performance of a model turbine in a variety of test facilities including two flumes and two towing tanks. They demonstrated that particularly for the Reynolds number ranges typically presented in the literature, turbine performance improves with increasing Reynolds number due to the

presence of the turbulent boundary layer which causes the flow to remain attached over a larger portion of the blade.

If the Reynolds number is used to describe the state of the flow over the blades, it makes the most sense to use the flow velocity the blade actually encounters, which is the relative velocity,  $U_{rel}$ . Similarly, the blade chord is the characteristic length that most readily describes the state of the flow over the blades. However, the relative velocity changes from blade root to tip and for tapered blades the chord length also changes. The question then becomes what relative velocity (i.e. blade radius) and chord length best describes the overall state of the flow over the turbine? It is advocated by the authors that the section of the blade that most contributes to power production should be the section at which the Reynolds number is defined. Blade Element Momentum Theory suggests the region around 0.7R contributes most significantly to power production [25]. A qualitative observation of the velocity deficit in the near wake of the turbine corroborates this being the radius at which the most power is extracted from the incoming flow. Viewed another way, sections closer to the hub have a relative velocity too low to contribute substantially to power production, and the contribution of sections near the tip are decreased by tip losses. Thus, it is advocated that the Reynolds number that best represents the achievement of dynamic similarity is calculated using the 0.7R chord length and relative velocity.

The NACA 633–618 airfoil section was selected for the present experiment, as opposed to the NACA 63–424 airfoil featured by RM1, because it has shown to be Reynolds number independent at  $Re \approx 1 \times 10^6$  [26]. A study conducted by the authors [20] demonstrated that at  $Re \approx 4.2 \times 10^5$  the NACA 633–618 airfoil was Reynolds number independent in lift and only slightly dependent in drag. Using the parameters specified previously, the Reynolds number for the present experiment was approximately  $4 \times 10^5$ , thus independent with respect to lift and slightly dependent with respect to drag. The impact of Reynolds number dependence in this case is likely a slightly lower prediction of power and thrust coefficient compared to the fully scale-independent turbine.

The equipment used to measure turbine performance parameters is shown in Fig. 3. Thrust and torque were measured using a Cussons R46 dynamometer, mounted in line with the turbine shaft. Shaft rotation speed and blade position were measured using a BEI Sensors H35 incremental optical encoder. The tip speed ratio was adjusted using a Placid Industries, Inc. H250 hysteresis brake attached to the output shaft. The brake also served to dissipate the

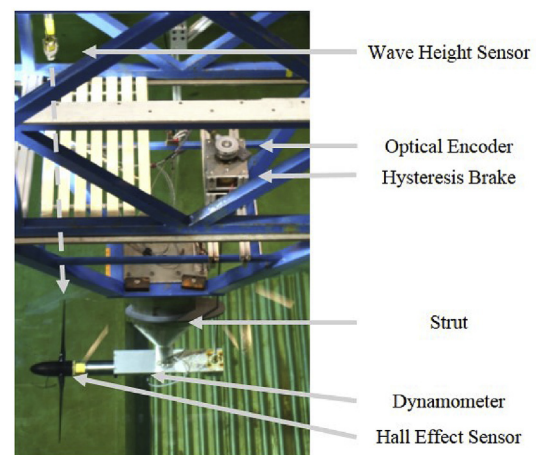


**Fig. 3.** Turbine performance measurement apparatus, viewed from above on the port side of the turbine, including the shaft speed encoder, magnetic brakes, surface-piercing strut, and dynamometer (submerged).



power produced by the turbine. All instruments were synchronized in time. Performance parameter (i.e. carriage speed, shaft speed, torque and thrust) sampling was conducted at a rate of 700 Hz. Each run, or traverse of the towing tank, provided 30–40 s of steady state data at a carriage speed of 1.68 m/s with the brake set to provide a tip speed ratio (TSR) of approximately 7.

Prior to the start of experiments, a survey with a single Nortek Vectrino Acoustic Doppler Velocimeter (ADV) was conducted 2D upstream of the rotor plane at a depth approximately equal to that of the turbine centerline to characterize the inflow conditions. It was found that streamwise turbulence intensity due to rotor passage was, after the minimum interval between runs (approximately 7 min), on order of 3%. This was found to be consistent with a more detailed tow tank ADV survey using this turbine described in Ref. [27]. Previous studies have reported similar turbulence intensities in flume tank experiments and suggest that this level of inflow (ambient) turbulence intensity represents a lower bound of the real condition values [17].

The tip speed ratio is the rotation speed of the turbine tip normalized by the free stream speed:

$$TSR = \frac{R\Omega}{U_{tow}} \quad (1)$$

where  $\Omega$  is the shaft speed, approximately 30 rad/s with 1.2% RMS of the mean value, and  $U$  is the carriage speed, measuring 1.68 m/s. A TSR of 7 was selected because it corresponds approximately to maximum power production, quantified by the power coefficient,  $C_p$ :

$$C_p = \frac{Q\Omega}{\frac{1}{2}\pi\rho U^3 R^2} \quad (2)$$

where  $Q$  is the torque and  $\rho$  is the density of fresh water at 17°C. The thrust coefficient,  $C_T$  is calculated similarly:

$$C_T = \frac{T}{\frac{1}{2}\pi\rho U^2 R^2} \quad (3)$$

Turbine performance in terms of power and thrust coefficient versus tip speed ratio is shown in Fig. 4. At maximum performance,  $C_p$  is approximately 0.43 with 1.9% RMS of the mean value and  $C_T$  is approximately 0.83 with 1.6% RMS of the mean value. The uncertainty analysis for the measured and calculated performance parameters for this turbine is included in Ref. [19], and are included as

error bars in Fig. 4.

The velocity field in the near wake of the model turbine was measured using 2-D particle image velocimetry (PIV), a technique used in previous studies (e.g. Refs. [15,16]). The PIV system featured a Quantel Evergreen, dual cavity Nd:YAG 200 mJ 532 nm laser capable of a repetition rate of 15 Hz. A 5 mm thick light sheet was formed using a 1000 mm spherical lens in combination with a 15 mm cylindrical lens. The camera was a TSI PowerView Plus 4 MP CCD camera with a resolution of 2048 × 2048 px providing a nominal resolution of 1.9 mm for a nominal 0.3 m by 0.3 m field of view. A 50 mm lens was used with remote focus and aperture adjustment. The camera had a maximum frame rate of 7.25 PIV image pairs per second (in Straddling Mode) and was positioned approximately 1.4 m from the light sheet to preclude interference of the submersible camera housing with the field of view. Image pair capture was triggered by a Hall Effect sensor mounted to the turbine hub so as to phase lock the image pairs with the blades positioned horizontally. The time between laser pulses was set to 1000  $\mu$ s, thus the blades rotated approximately 1.7° between images.

PIV images were captured and processed using TSI Insight 4G software. Camera exposure was set to 420  $\mu$ s and the aperture and autofocus were not changed once set initially to ensure a consistent field of investigation. At each position, 50 calibration images were taken and then averaged prior to calibration and de-warping yielding an average pixel size of approximately 157  $\mu$ m. Images were processed using a recursive Nyquist grid engine (50% overlap), and an FFT based correlation engine where the sub-pixel displacement was estimated using a Gaussian peak engine. Vector validation was conducted using the local median filter and bad vector replacement was accomplished by valid secondary peaks from the local correlation maps. Any remaining holes were filled using local interpolation and the resulting vector fields were then low-pass filtered using a narrow Gaussian filter to remove high-frequency noise (higher than the spatial resolution). The resulting particle displacements ranged from a minimum of approximately 2 px to a maximum of over 18 px, but the average displacement was approximately 8 px. Final interrogation spot size was set to 24 × 24 px providing a resolution of 12 px or 1.9 mm with less than 1% of vectors interpolated.

The PIV camera and light arm were contained in an in-house designed and manufactured system mounted directly to the towing carriage and submerged. The system, shown in Fig. 5, features

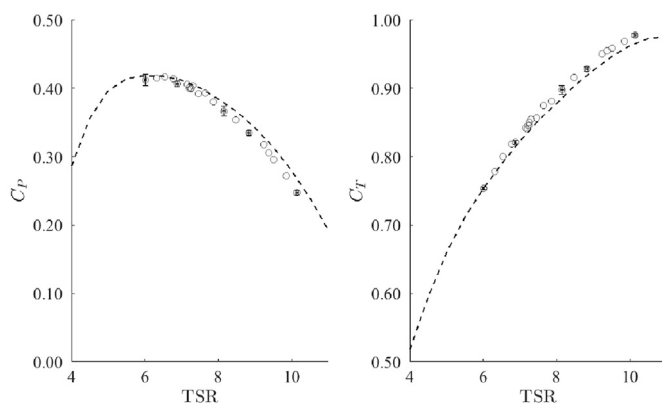


**Fig. 4.** (a) Power coefficient and (b) thrust coefficient versus tip speed ratio, adapted from Walker et al. [14] Open circles represent time-averaged experimental results. The solid line represents BEM predictions for a Reynolds number of 4e5. Error bars are included at TSR ≈ 6, 7, 8, 9 and 10.

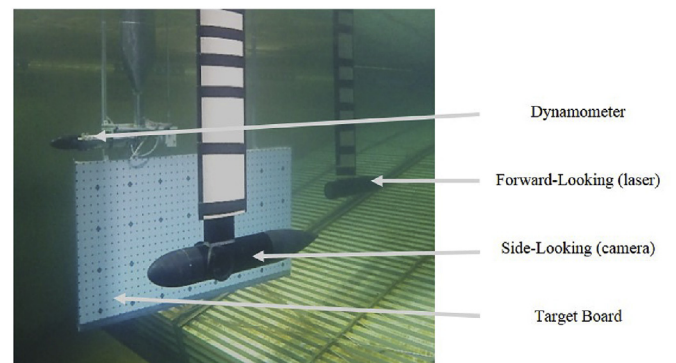


**Fig. 5.** An underwater view of the field of investigation including the dynamometer and turbine (turned so that the blades are horizontal), the target board (included in the image for reference but removed during data acquisition), the side-looking submersible which contained the camera and remote-focus electronics, and the forward-looking submersible which contained the laser light arm and laser sheet optics. During data acquisition, flow enters from the left. The entire submersible system was designed and manufactured in-house.

two submersible housings, one forward-looking and one side-looking, both streamlined to minimize flow disturbance in the measurement region. The laser or camera can be mounted interchangeably in either submersible, providing subsurface visualization capability in vertical planes parallel to both the long and short axes of the towing tank.

For all observations, the submersibles remained fixed to the towing carriage and the turbine was translated to change the field of view. The side-looking submersible was mounted 1.7D from the field of view and the forward-looking submersible was mounted at least 2.6D from the field of view with the turbine in the aft-most position. The minimum turbine tip depth from the free surface was 0.5D. Previous studies [e.g. Ref. [28]] have demonstrated this depth to be sufficiently deep so as not to deform the free surface or impact turbine performance characteristics.

The streamwise direction, parallel to the long axis of the towing tank, was defined as the  $x$ -direction with the positive direction oriented downstream (opposite the direction of towing carriage travel). The vertical direction was defined as the  $z$ -direction with positive directed upward. The corresponding velocity vectors are denoted  $u$  and  $w$ , respectively. The origin for position reference was defined as the center of the turbine hub at the same streamwise position as the turbine blades (Fig. 6). PIV measurements were performed along the  $x$ - $z$  plane, parallel to and beneath the output shaft of the turbine as shown in Fig. 6. Fields of view extended from approximately 0.11 m (0.14D) upstream of the turbine tip path to 1.57 m (1.97D) downstream and extending downward from beneath the turbine output shaft to a distance of 0.68 m (0.85D). Each individual field of view measured approximately 0.3 m by 0.3 m with 0.05 m overlap between adjacent fields (Fig. 6). Measurements were made in a region of the wake that did not include the strut or support equipment.

The seed particles used in this experiment were Potters Industries SpheriCell® 110p8 hollow glass microspheres. The mean particle size was 12  $\mu\text{m}$  and the density ranged from 1.05 to 1.15  $\times 10^3 \text{ kg/m}^3$ . The seed particles were distributed using a “rake,” approximately the same overall size as the turbine diameter. The towing speed and rake tine diameter were selected to maximize mixing. Perforated tubing was attached to the rake tines through which the seed particles were pumped. The rake was towed the length of the tank each day prior to the start of data collection and the process was repeated as needed as signal quality degraded. Seed particle concentration was approximately 0.5 kg per 200 L container of water and the volumetric flow rate for the seed/water mixture was approximately 0.5 L/s.

For each field of view position approximately 1000 steady-state

(i.e. constant carriage speed) realizations were collected over the course of five runs with each run yielding approximately 200 realizations. Image capture was initiated using a Hall Effect sensor on the turbine hub such that each image pair was captured when the two blades were oriented horizontally (i.e. parallel to the free surface). Thus the resulting flow fields are phase locked at a single blade phase,  $\phi_b$ . In order to verify that 1000 realizations were sufficient to provide a statistically-converged phase average, a cumulative average velocity components including 200, 400, etc. realizations were calculated and plotted for a single field of view (Fig. 7). The selected field of view, located furthest downstream (1.6  $< x/D < 2.0$ ), was chosen because it included the shear layer and was in the region where the vortex meandering was the most pronounced, thus representing the likely worst-case-scenario in terms of repeatability of velocity measurements. The phase average velocity components were normalized by the towing carriage speed. Both components are shown to converge to approximately 0 after 1000 realizations indicating a statistically-converged phase average (i.e.  $\overline{u_i} = 0$ ).

An uncertainty analysis was conducted using the image matching methodology developed by Sciacchitano, Wieneke, and Scarano [29]. The algorithm was applied to images from the same field of view shown in Fig. 7. The maximum error was less than 2% for both velocity components, quoted at 60% confidence. It should be noted that the peak-locking errors and truncation errors in time are not detected with the image matching approach. However, the particle image diameter was greater than 2 px, thus peak-locking was not anticipated.

A transform was created to map the center of each field of view, indicated by the center of the fiducial marker (Fig. 6), to the flow field origin. All  $x$  and  $z$  coordinates for each field of view were then transformed and plotted simultaneously. For adjacent fields of view, the  $x$  and  $z$  coordinates were not identical in the overlap region. When plotted, this artifact is manifested as a discontinuity in the overlapping region.

### 3. Results

The tip vortices shed by the turbine blades are one of the most prominent features of the wake. They serve as useful markers for observing the evolution of the shear layer. More fundamentally, however, the interaction between adjacent helical vortex filaments is thought to be the primary mechanism for initiating momentum transport into and re-energization of the wake [9,12,14,15,30]. Characterization is therefore critical to informing this discussion.

The  $\lambda_{ci}$  criterion developed by Zhou et al. [31] was used to estimate the vortex center position. However, using this method, the centroid could only be found within the measurement resolution of the interrogation window, approximately 1.9 mm. Moreover, as stated by Bhagwat and Ramasamy [32], measurement in the region of the core of a vortex is inherently difficult due to a seed particle void created by the strong swirling motion and variations in local velocity due to turbulence. Thus, using the methodology they developed for helicopter rotor research a vortex model was fit to the experimental observations in order to more accurately identify the vortex properties. Three vortex models – the Lamb-Oseen model generally used for laminar vortices, the Scully Vortex model generally representative of turbulent vortices, and the model developed by Vatis et al. generally describing vortices in the transition region, all described by Leishman [33] – were applied to each vortex in each realization using a non-linear least-squares fit algorithm as described in Ramasamy, Paetzel, and Bhagwat [34]. The fit was applied to a subregion of 21 by 21 elements (approximately 40 mm by 40 mm) centered on the location of maximum  $\lambda_{ci}$ . The core radii were then averaged for each vortex in each

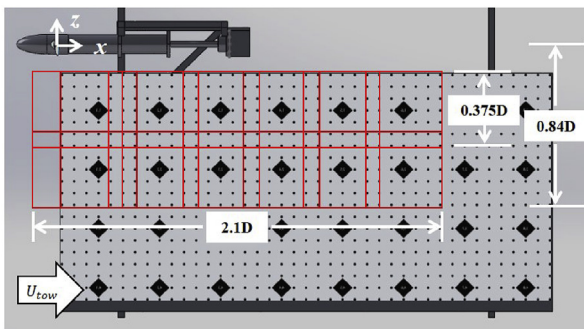


**Fig. 6.** A schematic of the field of investigation. The red squares encompass each of the fields of view (14 total), each centered on a fiducial marker (solid diamond) and measuring approximately 30 cm by 30 cm. Flow entered from the left. (For interpretation of the references to colour in this figure legend, the reader is referred to the Web version of this article.)

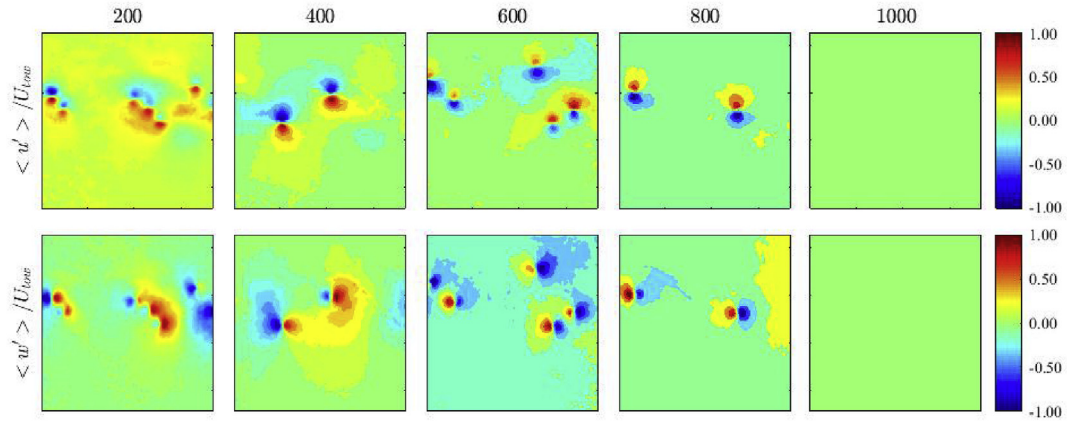


**Fig. 7.** Cumulative average fluctuating velocity for  $u'$  (first row) and  $w'$  (second row) for the number of realizations indicated in the column header. Values are normalized by the towing carriage speed,  $U_{tow}$ . Field of view located  $1.6 < x/D < 2.0$  and  $-0.45 < z/D < -0.85$  from the turbine origin.

realization. The resulting average vortex core diameter was approximately 0.7 times the tip chord length of 24 mm (18 mm or 9 elements) in agreement with [7]. The model selected, of the three that were fit to a particular vortex, was based on which of the models produced the smallest residual norm in consideration for the changing nature of the vortices with streamwise distance. Each of the three models have been shown previously to predict the same centroid position [34]. This was also observed in the present study. Model results were compared to experimental results and are presented in Fig. 8.

### 3.1. Mean flow

Fig. 8a shows the phase-averaged streamwise velocity,  $\langle u(x, z, \phi_b) \rangle$  normalized by the carriage speed,  $U_{tow}$  for the entire field of investigation extending from 0.14D upstream of the turbine tip path to 1.97D downstream and to a depth beneath the output

shaft of 0.85D. The velocity decreases just upstream of the turbine to approximately 75% of the towing carriage speed, the result of the slight rise in the static pressure of the free stream flow approaching the turbine. The tip vortices are rotating counter-clockwise (i.e. in the negative  $y$ -direction). Wake expansion, indicated by the position of the vortex centers, is modeled reasonably well by a 1/3 power law expansion (i.e.  $z = ax^{1/3} + b$ ) with an  $R^2_{adj}$  correlation value of 0.95. This agrees well with theory and observations from horizontal axis wind turbine studies as well as the marine current turbine literature (e.g. Refs. [4,9]). Inside the wake, the velocity deficit is largest coincident with 0.3–0.4D radial location from the output shaft (approximately 0.7R). The streamwise velocity reaches a minimum value, for this field of investigation, of approximately 1/3 the free stream flow velocity at approximately 2D downstream as predicted by Froude and previously observed (e.g. Refs. [6,11]). The maximum velocity deficit occurs downstream of the turbine because the static pressure, at its lowest immediately downstream

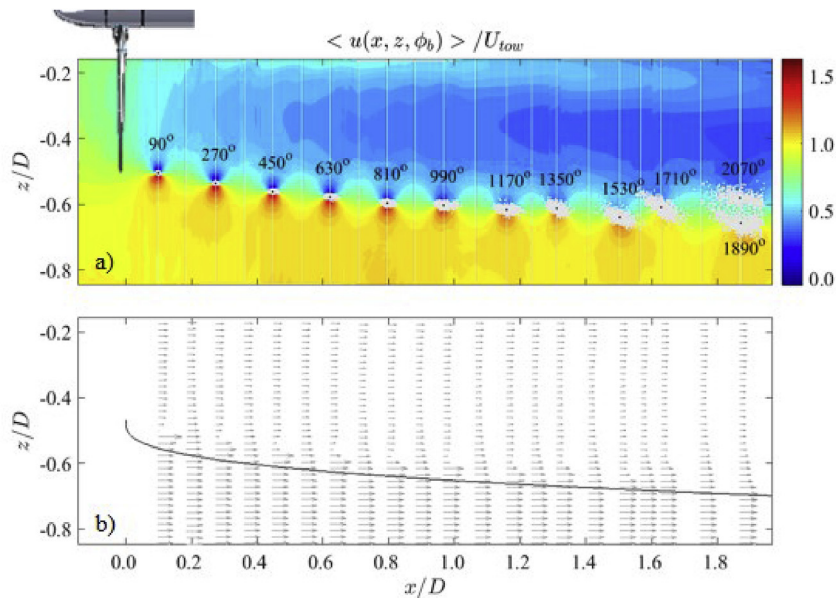


**Fig. 8.** (a) Phase averaged velocity in the streamwise direction for the entire field of investigation. The annotations above each vortex indicate the wake age in degrees of turbine rotation. Light gray dots indicate vortex center positions for approximately 14,000 realizations. The black dots indicate the mean centroid position. The vertical lines indicate the position of the velocity profile shown in (b). The free stream velocity is from left to right and the turbine is shown to scale in the upper left-hand corner. Figure (b) shows the streamwise vertical velocity profiles for vertical cuts located at the mean centroid positions and positions between adjacent vortices. The solid line is a 1/3 power-law fit to the  $0.99U_{tow}$  contour representing the wake boundary.



of the turbine, recovers by extracting energy from the wake at the expense of velocity. Not accounting for losses or energy transferred to the wake from the mean flow, the streamwise location of the maximum velocity deficit marks the location where the static pressure has returned to that of the pressure far upstream.

Vortex meandering or *aperiodicity* as it will be referred to in the present discussion is defined as the random variations in the spatial location of the vortex centers. This is shown to increase with increasing wake age or the angular travel, in degrees, of the blade that created the helical vortex filament. Aperiodicity is thought to be the first manifestation of helical instability [15]. By approximately 1.6D, the aperiodicity is so pronounced as to make it difficult to identify individual vortices in a phase-locked regime. However, the separation between the two point clouds downstream of  $x/D = 1.8$  indicates that a level of coherency is maintained. A detailed discussion of vortex characteristics is included in the next section.

The vertical lines on Fig. 8a correspond to the phase-averaged streamwise velocity profiles shown in Fig. 8b. These vertical “cuts” pass through each mean vortex center position and at the midpoint between adjacent vortices. The wake width,  $\delta$  indicated by the dark gray line in Fig. 8b can be defined using a variety of methods as described in Ref. [9]. It is defined here as  $\langle u(x, z, \phi_b) \rangle / U_{tow} \approx 0.99$ . The wake width was calculated from the velocity profiles passing between the mean vortex center positions. The number of velocity vectors shown has been reduced by a factor of 10 for clarity.

For further confirmation of mean flow measurements, the drag on the turbine, approximately equal to the thrust, was calculated in terms of the deficit of momentum flux across in the wake at a distance of approximately 1.4D downstream (profile shown in Fig. 8b) where wake expansion had effectively ceased. The wake was also assumed to be axisymmetric. Since the field of investigation was displaced from the output shaft by approximately 0.16D (i.e. no data were recorded in this region) the velocity profile was estimated to be constant at the observed velocity nearest the output shaft. This is likely a low estimate since the streamwise flow in this region is likely to be slower. The calculated value of the wake drag was found to agree within approximately 5% of the independently-measured thrust coefficient value of 0.84, giving confidence in the observed results.

Fig. 9a shows the phase-averaged vertical velocity,  $\langle w(x, z, \phi_b) \rangle$  also normalized by the carriage speed,  $U_{tow}$ . Just upstream of the turbine, there is a small negative vertical velocity component in the negative  $z$ -direction (i.e. radially outward), the result of wake expansion beginning upstream of the turbine. Wake expansion, as described by the vertical velocity, persists until approximately 1D after which there is very little vertical velocity outside of the vortices as indicated by the flattening of the wake boundary. This is consistent with what was shown by Chamorro et al. [4] and indicates that the assumption made in blade element momentum theory that the fluid inside the stream-tube does not interact with the flow outside the stream-tube is reasonable. The counter-clockwise rotation of the vortices is also clearly shown. The signature of several blade root vortices also appear in the upper left-hand corner of Fig. 9a.

In Fig. 9b the phase-averaged vertical velocity is shown along the wake boundary, giving a sense of the magnitude of the flow across the wake boundary. Keeping in mind that velocities shown above are phase averaged over nearly a thousand realizations and that the wake boundary location is estimated, the figure approximates the swirl velocity profile for a horizontal “cut” through each of the tip vortices. It appears that the swirl velocity is decreasing with downstream distance. It also appears that the vortex core radius (i.e. half the distance between adjacent peaks) is increasing with streamwise distance, however, this is primarily a result of

increasing aperiodicity, rather than core radius dilation, as discussed in a later section. Both Fig. 9a and b indicate that aside from the negative vertical velocity associated with wake expansion within the first diameter, there is very little vertical velocity across the wake boundary, potentially indicating little exchange between the mean flow and the wake in terms of bulk fluid motion.

### 3.2. Vortex characterization

As shown previously, the turbine tip vortices feature prominently in any visualization of the phase-averaged wake and interaction between adjacent vortex helices is thought to be the primary mechanism for initiating breakdown of the coherent wake structure and subsequent wake re-energization [12,14,15,30]. In Fig. 10a, the vortex center positions for each realization are again indicated by the light gray dots and the average center position is marked with a black dot. The mean aperiodicity,  $\bar{r}_A$  or variability of vortex center position from the mean position, is defined as:

$$\bar{r}_A = \frac{1}{N} \sum_{k=1}^N \sqrt{(x_{c,k} - \bar{x}_c)^2 + (z_{c,k} - \bar{z}_c)^2} \quad (4)$$

The aperiodicity was calculated for each vortex over all associated realizations. The results are shown on the left y-axis of Fig. 10b. At a wake age of 90° the vortex center positions are tightly grouped and thus the aperiodicity is low (i.e. the vortex center positions are highly periodic). As wake age increases aperiodicity also increases, indicated qualitatively by the expanding scatter of the gray dots in Fig. 10a and quantitatively by the trend shown on the left y-axis of Fig. 10b. On the right y-axis of Fig. 10b it is shown that at wake ages less than approximately 990° vortex center spacing was fairly constant at 0.18D. However, for wake ages greater than 990° mean streamwise spacing increases and decreases alternately. This likely indicates the start of mutual induction. The interaction becomes more pronounced as the 1350° vortex is shifted upward in the positive  $z$ -direction. The upward movement of the vortex is likely due to interaction between the upturning flow on the downstream side of the 1170° vortex and the down-turning flow on the upstream side of the 1350° vortex. Moreover, as the 1350° vortex is pushed into the slower-moving wake, it is slowed in the streamwise direction and its presence forces the 1170° vortex down into the faster-moving flow, furthering the counter-clockwise rotation of the now-grouped helices. This phenomenon is also shown in similar studies [12,15]. The interaction is even more pronounced for the 1530° and 1710° vortices, which are clearly entangled and rotating around a common saddle point in a motion classically referred to as *leapfrogging*. The scatter associated with aperiodicity is also increasingly inclined relative to the horizontal, a manifestation of the underlying shear layer. In the case of the vortices detected downstream of approximately 1.7D, the aperiodicity was so great that individual vortices could not clearly be identified as being of a particular wake age. However, a close inspection shows that there is a slim, horizontally-oriented region of low vortex center density, suggesting that the 1890° vortex is being subducted beneath the 2070° vortex such that the two adjacent helices are now oriented vertically having gone through 90° of rotation together.

The vortex core radius,  $r_c$  was calculated for each vortex in each realization using two cuts – one horizontal (0°) and one vertical (90°) – through the element nearest the vortex center indicated by the vortex model. Each cut provided a velocity profile from which the vortex core radius and peak swirl velocity were calculated as discussed in Ramasamy et al. [35]. The resultant core radius values were averaged for each vortex and are shown as closed circles

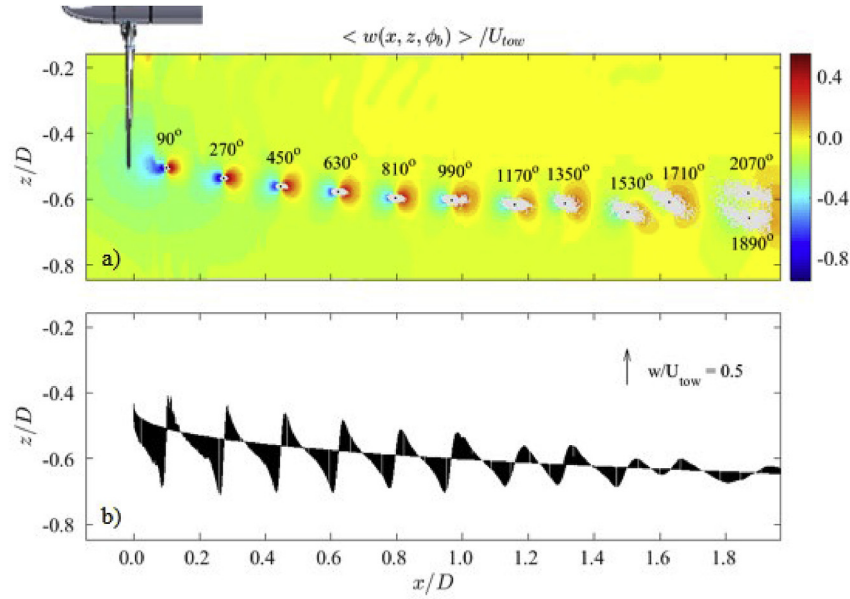


**Fig. 9.** (a) Phase-averaged velocity for the entire field of investigation in the vertical direction. The annotations above each vortex indicate the wake age in degrees of turbine rotation. The light gray dots markers indicate vortex center positions for approximately 14,000 realizations. The black dots indicate the mean centroid position. The free stream velocity is from left to right, and the turbine is shown to scale in the upper left-hand corner. Figure (b) shows the vertical velocity profile plotted along the wake boundary, shown in Figure (a). The black arrows indicate the magnitude of the vertical velocity at that position, according to the scale indicated in the upper right-hand corner of the figure.

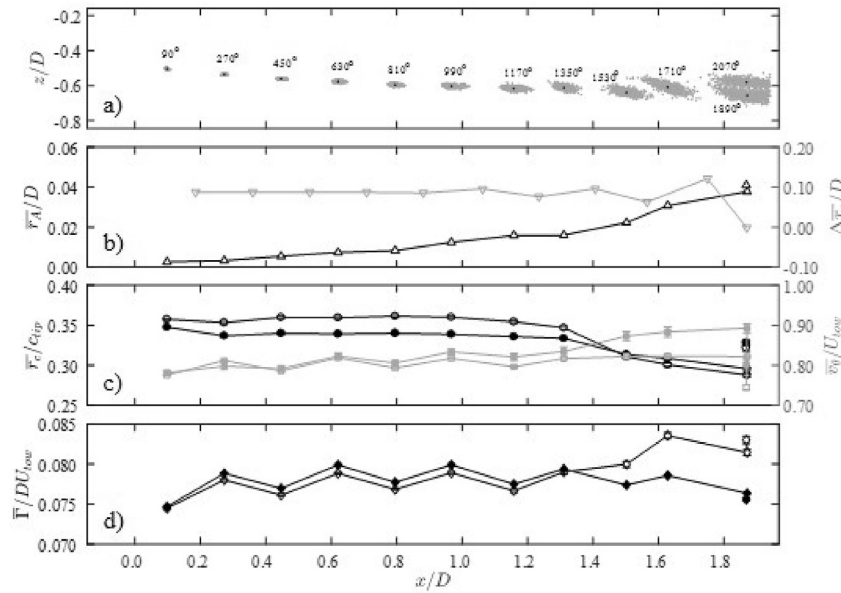


**Fig. 10.** (a) Vortex center positions for each traceable vortex. The light gray markers represent the vortex centroid positions for each realization. The black markers represent the average centroid position. The left y-axis of Figure (b) shows the aperiodicity non-dimensionalized by the turbine diameter. The right y-axis shows the streamwise spacing between adjacent mean centroid positions. The left y-axis of Figure (c) shows the vortex core radius calculated from experimental data (closed circles) and determined from the vortex model fitting methodology (open circles). Both are normalized by the turbine blade tip chord length. The right y-axis of Figure (c) shows the mean swirl velocity calculated from experimental data (closed squares) and determined from the vortex fitting methodology (open squares). Figure (d) shows the average vortex circulation calculated for only the vortex core region from experimental data (closed diamonds) and determined for the entire vortex using the model fitting methodology (open diamonds). Both are non-dimensionalized by the turbine diameter and the towing carriage speed. Error bars are included in (c) and (d) with bar length equal to two times the standard deviation of the associated quantities, quoted at 95% confidence.

plotted on the left y-axis of Fig. 10c. The vortex core radii, calculated using the vortex model fit methodology described in a previous section, were also averaged for each vortex and also plotted on the left y-axis of Fig. 10c as open circles for comparison. The two are shown to be in close agreement (maximum difference of 6%) giving confidence in the model results. The radii are non-dimensionalized

by the turbine blade tip chord length,  $c$  and indicate that vortex core diameter is of the same order of magnitude, as previously observed [4,15]. Vortex core radius is fairly constant at approximately  $0.35c$ , in reasonable agreement with previous studies [15] until a downstream distance of  $x/D \approx 1$ , after which the core radius begins to decrease.



On the right y-axis of Fig. 10c the mean peak swirl velocity is shown for each vortex with model results indicated with open squares and experimental results shown with closed squares. Again, there is close agreement between model predictions and experimental results (maximum 5% difference). The alternating swirl velocity values may be due to a slight difference blade manufacturing or base pitch. It appears that in the region of interaction,  $x/D > 1$ , the core radii decrease slightly as the swirl velocity increases slightly. Interestingly, this is contrary to what was observed in Sherry et al. [15] and may be a Reynolds number effect as low Reynolds number contributes to enhanced diffusion of vortical structures.

Fig. 10d shows the mean circulation for each vortex, normalized by the turbine diameter and towing carriage speed, with the open diamond symbols representing the model output and the closed diamonds representing the experimental results. The circulation was calculated from the experimental data using the line integral along the subregion perimeter. The area integral value was also calculated for the subregion and was found to be in close agreement with the line integral, thus only one is shown. Neither data set shows significant variation in the near wake. Experimental values are approximately 70% of theoretical values. This is because model values include all circulation associated with the vortex, assumed to be in otherwise quiescent flow. Experimental values only include the vorticity in the vortex core which accounts for approximately 70% of the total vorticity in laminar vortices and 40% in turbulent vortices [15,34]. Indeed, the experimental circulation values for the present experiment are approximately 70% of the model values, suggesting that the vortices in this region are primarily laminar. There is also a slight disagreement between the two results in the interaction region at  $x/D > 1.4$ . This is likely due to the model assumption that the surrounding flow is quiescent.

#### 4. Conclusions

A study was conducted of the near-wake of a two-bladed, 0.8 m diameter, near-Reynolds number independent axial-flow hydrokinetic turbine in steady flow conditions. The field of investigation extended from approximately 0.1D upstream of the turbine to 2.0D downstream, and radially outward to a distance of 0.85D. High resolution flow field observations were made using 2-D planar PIV enclosed in a submersible housing system. Phase-averaged flow field results support many previous observations made for smaller-scale models. These include the slowing of the flow just upstream of the turbine to 75% of the free stream velocity due to the increase in static pressure, wake expansion well-described by the 1/3 power of the streamwise distance, and the velocity deficit reaching a maximum of 2/3 the free stream velocity. Turbine blade root vortices were also observed but to a very limited extent given the limits of the field of investigation.

Tip vortex characterization techniques were applied to calculate relevant vortex parameters. Spacing of adjacent vortex filaments was relatively constant as was vortex core radius to a streamwise distance of approximately 1.0D. Further downstream vortex interaction and mutual induction were observed followed by the first 90° rotation of leapfrogging, the phenomenon that likely initiates wake re-energization.

In addition to providing large scale data for computational model validation, the present work provides a basis for comparison to follow-on studies focused on the influence of surface gravity waves on wake development.

#### Acknowledgements

Funding for this research was provided by the Office of Naval

Research. The authors would like to thank James Duncan for his suggestions and insights with regard to the scope and conduct of the experiment, Julio Barros for his assistance with setting up the PIV system, Joseph Milluzzo for his assistance with wake analysis, and the staff of the U.S. Naval Academy Hydromechanics Laboratory for their contributions in designing, building, and testing of the marine hydrokinetic turbine. We would also like to thank the Offshore Wind and Ocean Power Systems research group at NREL for their support and collaboration and the referees who reviewed and improved this manuscript.

#### References

- [1] W.A. Hermann, Quantifying global exergy resources, *Energy* 31 (12) (2006) 1349–1366, <https://doi.org/10.1016/j.energy.2005.09.006>.
- [2] Z. Zhou, M. Benbouzid, J.-F. Charpentier, F. Scullier, T. Tang, Developments in large marine current turbine technologies – a review, *Renew. Sustain. Energy Rev.* 71 (November 2016) (2017) 852–858, <https://doi.org/10.1016/j.rser.2016.12.113>. URL, <http://www.sciencedirect.com/science/article/pii/S1364032116311698>.
- [3] T. Heinrichs, DOE Reference Model Project Fact Sheet, 2015. URL, <http://energy.sandia.gov/energy/renewable-energy/water-power/technology-development/reference-model-project-rmp/>.
- [4] L. P. Chamorro, D. R. Troolin, S. J. Lee, R. E. A. Arndt, F. Sotiropoulos, Three-dimensional flow visualization in the wake of a miniature axial-flow hydrokinetic turbine, *Exp. Fluids* 54 (2). doi:10.1007/s00348-013-1459-9.
- [5] I.V. Naumov, V.V. Rahmanov, V.L. Okulov, C.M. Velte, K.E. Meyer, R.F. Mikkelsen, Flow diagnostics downstream of a tribladed rotor model, *Thermophys. Aeromechanics* 19 (2) (2012) 171–181, <https://doi.org/10.1134/S0869864312020011>. URL, <https://doi.org/10.1134/S0869864312020011>.
- [6] V.L. Okulov, I.N. Naumov, I. Kabardin, R. Mikkelsen, J.N. Sørensen, Experimental investigation of the wake behind a model of wind turbine in a water flume, *J. Phys. Conf.* 555 (1) (2014), 012080, <https://doi.org/10.1088/1742-6596/555/1/012080>. URL, <http://stacks.iop.org/1742-6596/555/i=1/a=012080?key=crossref.ede49cc55a4cb2d8f41cd07aba4b7302>.
- [7] L.P. Chamorro, C. Hill, S. Morton, C. Ellis, R.E.A. Arndt, F. Sotiropoulos, On the interaction between a turbulent open channel flow and an axial-flow turbine, *J. Fluid Mech.* 716 (2013) 658–670, <https://doi.org/10.1017/jfm.2012.571>.
- [8] F. Maganga, G. Germain, J. King, G. Pinon, E. Rivoalen, Experimental characterisation of flow effects on marine current turbine behaviour and on its wake properties, *IET Renew. Power Gener.* 4 (6) (2010) 498–509, <https://doi.org/10.1049/iet-rpg.2009.0205>.
- [9] J. Allo, C. Del Frate, D. Dhome, F. Di Felice, F. Alves Pereira, Slipstream dynamics of a tidal turbine, in: *Proceedings of the 12th European Wave and Tidal Energy Conference*, Cork, Ireland, 2017, pp. 2–11.
- [10] P. Mycek, B. Gaurier, G. Germain, G. Pinon, E. Rivoalen, Experimental study of the turbulence intensity effects on marine current turbines behaviour. Part I: one single turbine, *Renew. Energy* 66 (2014) 729–746, <https://doi.org/10.1016/j.renene.2013.12.036>. URL, <https://doi.org/10.1016/j.renene.2013.12.036>.
- [11] S.C. Tedds, I. Owen, R.J. Poole, Near-wake characteristics of a model horizontal axis tidal stream turbine, *Renew. Energy* 63 (2014) 222–235, <https://doi.org/10.1016/j.renene.2013.09.011>. URL, <https://doi.org/10.1016/j.renene.2013.09.011>.
- [12] L.E. Lignarolo, D. Ragni, F. Scarano, C.J. Simão Ferreira, G.J. van Bussel, Tip-vortex instability and turbulent mixing in wind-turbine wakes, *J. Fluid Mech.* 781 (2015) 467–493, <https://doi.org/10.1017/jfm.2015.470>.
- [13] S.E. Widnall, The stability of a helical vortex filament, *J. Fluid Mech.* 54 (04) (1972) 641, <https://doi.org/10.1017/S0022112072000928>.
- [14] M. Felli, R. Camussi, F. Di Felice, Mechanisms of evolution of the propeller wake in the transition and far fields, *J. Fluid Mech.* 682 (2011) 5–53, <https://doi.org/10.1017/jfm.2011.150>.
- [15] M. Sherry, A. Nemes, D. Lo Jacono, H. M. Blackburn, J. Sheridan, The interaction of helical tip and root vortices in a wind turbine wake, *Phys. Fluids* 25 (11). doi:10.1063/1.4824734.
- [16] L.E.M. Lignarolo, D. Ragni, C. Simão Ferreira, G. van Bussel, Kinetic energy entrainment in wind turbine and actuator disc wakes: an experimental analysis, *J. Phys. Conf.* 524 (1) (2014), 012163, <https://doi.org/10.1088/1742-6596/524/1/012163>. URL, <http://iopscience.iop.org/1742-6596/524/1/012163>.
- [17] P. Mycek, B. Gaurier, G. Germain, G. Pinon, E. Rivoalen, Experimental study of the turbulence intensity effects on marine current turbines behaviour. Part II: two interacting turbines, *Renew. Energy* 68 (2014) 876–892, <https://doi.org/10.1016/j.renene.2013.12.048>. URL, <https://doi.org/10.1016/j.renene.2013.12.048>.
- [18] Molland Bahaj, Batten Chaplin, *Power and Thrust Measurements of Marine Current turbines*, Pdf, 2007.
- [19] E.E. Lust, L. Luznik, K.A. Flack, J.M. Walker, M.C. Van Benthem, The influence of surface gravity waves on marine current turbine performance, in: *10th European Wave and Tidal Energy Conference*, Aalborg 3–4 (m), 2013, pp. 27–40, <https://doi.org/10.1016/j.ijome.2013.11.003>. URL, <http://linkinghub.elsevier.com/retrieve/pii/S2214166913000295>.

- [20] J.M. Walker, K.A. Flack, E.E. Lust, M.P. Schultz, L. Luznik, Experimental and numerical studies of blade roughness and fouling on marine current turbine performance, *Renew. Energy* 66 (2014) 257–267, <https://doi.org/10.1016/j.renene.2013.12.012>. URL <https://doi.org/10.1016/j.renene.2013.12.012>.
- [21] S. Rose, A. Good, M. Atcheson, G. Hamill, C. M. Johnstone, P. MacKinnon, D. Robinson, A. Grant, T. Whittaker, Investigating experimental techniques for measurement of the downstream near wake of a tidal turbine, *EWTEC 2011 Proceedings*.
- [22] Naumov\_et-al\_2-2012\_V.
- [23] L.P. Chamorro, R.E.A. Arndt, F. Sotiropoulos, Reynolds number dependence of turbulence statistics in the wake of wind turbines, *Wind Energy* 15 (5) (2012) 733–742, <https://doi.org/10.1002/we.501>.
- [24] B. Gaurier, G. Germain, J.V. Facq, C.M. Johnstone, A.D. Grant, A.H. Day, E. Nixon, F. Di Felice, M. Costanzo, Tidal energy "round Robin" tests comparisons between towing tank and circulating tank results, *Int. J. Marine Energy* 12 (2015) 87–109, <https://doi.org/10.1016/j.ijome.2015.05.005>. URL <https://doi.org/10.1016/j.ijome.2015.05.005>.
- [25] J.F. Manwell, J.G. McGowan, A.L. Rogers, *Wind Energy Explained: Theory, Design and Application*, John Wiley & Sons, 2010.
- [26] S. Miley, A Catalog of Low Reynolds Number Airfoil Data for Wind Turbine Applications, Tech. Rep., Texas A&M University, College Station, 1982. URL, <http://wind.nrel.gov/public/library/3387.pdf>.
- [27] L. Luznik, K.A. Flack, E.E. Lust, K. Taylor, The effect of surface waves on the performance characteristics of a model tidal turbine, *Renew. Energy* 58 (2013) 108–114, <https://doi.org/10.1016/j.renene.2013.02.022>. URL <https://doi.org/10.1016/j.renene.2013.02.022>.
- [28] A.S. Bahaj, L.E. Myers, R.I. Rawlinson-Smith, M. Thomson, The effect of boundary proximity upon the wake structure of horizontal Axis marine current turbines, *J. Offshore Mech. Arctic Eng.* 134 (2) (2012), 021104, <https://doi.org/10.1115/1.4004523>. URL, <http://eprints.soton.ac.uk/75271/%5Cnhttp://offshoremechanics.asmedigitalcollection.asme.org/article.aspx?articleid=1457736>.
- [29] A. Sciacchitano, F. Scarano, B. Wieneke, PIV uncertainty quantification by image matching, *Meas. Sci. Technol.* 24 (2013) 1–20, <https://doi.org/10.1088/0957-0233/24/4/045302>.
- [30] A. Nemes, M. Sherry, D.L. Jacono, H.M. Blackburn, J. Sheridan, Evolution and breakdown of helical vortex wakes behind a wind turbine, *J. Phys. Conf.* 555 (1) (2014), 012077, <https://doi.org/10.1088/1742-6596/555/1/012077>. URL, <http://stacks.iop.org/1742-6596/555/i=1/a=012077>.
- [31] J. Zhou, R.J. Adrian, S. Balachandral, T.M. Kendall, Mechanisms for generating coherent packets of hairpin vortices in channel flow, *J. Fluid Mech.* 387 (1999), <https://doi.org/10.1017/S002211209900467X>. S002211209900467X, [http://www.journals.cambridge.org/abstract\\_S002211209900467X](http://www.journals.cambridge.org/abstract_S002211209900467X). URL.
- [32] M.J. Bhagwat, M. Ramasamy, Effect of tip vortex aperiodicity on measurement uncertainty, *Exp. Fluid* 53 (5) (2012) 1191–1202, <https://doi.org/10.1007/s00348-012-1348-7>.
- [33] G.J. Leishman, *Principles of Helicopter Aerodynamics*, Cambridge University Press, 2006.
- [34] M. Ramasamy, R. Paetzel, M. J. Bhagwat, Aperiodicity Correction for Rotor Tip Vortex Measurements, American Helicopter Society 67th Annual Forum. URL <http://hdl.handle.net/2060/20110014252>.
- [35] M. Ramasamy, B. Johnson, T. Huisman, J.G. Leishman, Digital particle image velocimetry measurements of tip vortex characteristics using an improved aperiodicity correction, *J. Am. Helicopter Soc.* 54 (2009) 1–13, <https://doi.org/10.4050/JAHS.54.012004>.